

Acoustic singular surfaces in an exponential class of inhomogeneous gases: A new numerical approach based on Krylov subspace spectral methodologies*

B. Rester^a, J. V. Lambers^a, P. M. Jordan^{b,*}

^a*School of Mathematics and Natural Sciences, The University of Southern Mississippi, Hattiesburg, MS 39406, USA*

^b*Acoustics Division, U.S. Naval Research Laboratory, Stennis Space Center, MS 39529, USA*

Abstract

We investigate the propagation of acoustic singular surfaces, specifically, linear shock waves and nonlinear acceleration waves, in a class of inhomogeneous gases whose ambient mass density varies exponentially. Employing the mathematical tools of singular surface theory, we first determine the evolution of both the jump amplitudes and the locations/velocities of their associated wave-fronts, along with a variety of related analytical results. We then turn to what have become known as Krylov subspace spectral (KSS) methods to numerically simulate the evolution of the full waveforms under consideration. These are not only performed quite efficiently, since KSS allows the use of ‘large’ CFL numbers, but also quite accurately, in the sense of capturing theoretically-predicted features of the solution profiles more faithfully than other time-stepping methods, since KSS customizes the computation of the components of the solution corresponding to the different frequencies involved. The presentation concludes with a listing of possible, acoustics-related, follow-on studies.

Keywords: Krylov subspace spectral methods, inhomogeneous gases, singular surfaces, Laplace transform, nonlinear acoustics

1. Introduction

For the general case of an inhomogeneous fluid undergoing isentropic¹ flow, the (compressible) Euler system assumes the form [1]:

$$D\rho/Dt = -\rho(\nabla \cdot \mathbf{v}), \quad (1a)$$

$$\rho D\mathbf{v}/Dt = -\nabla p + \rho\mathbf{B}, \quad (1b)$$

$$Dp/Dt = c^2 D\rho/Dt. \quad (1c)$$

Here, in Cartesian coordinates, $\mathbf{v} = (u, v, w)$ is the velocity vector; $\rho(> 0)$ is the mass density; $p(> 0)$ is the thermodynamic pressure; $\mathbf{B} = \mathbf{B}(x, y, z)$ is the external (per unit mass) body force vector; D/Dt is the material derivative; and the (thermodynamic) variable $c(> 0)$ denotes the sound speed. If the fluid in question is a gas, specifically, a *perfect gas*, then $c^2 = \gamma p/\rho$ and p, ρ , and θ satisfy the following special case of the *ideal gas law* [37, § 2.5]:

$$p = (c_p - c_v)\rho\theta \quad (c_p, c_v := \text{const.}). \quad (2)$$

Here, $\theta(> 0)$ is the absolute temperature; $c_p > c_v > 0$ are the specific heats at constant pressure and volume, respectively; and $\gamma = c_p/c_v$, where $\gamma \in (1, 5/3]$ for perfect gases.

To simplify the analyses to be performed, we hereafter limit our attention to propagation in (perfect) gases and, moreover, always take the ambient state of the gas in question to be *quiescent* [28, p. 14]; i.e., while p_a, ρ_a, θ_a , and η_a

*Distribution Statement A: Approved for public release. Distribution is unlimited.

*Corresponding author.

¹That is, $D\eta/Dt = 0$, where η is the specific entropy; see, e.g., Thompson [37, p. 60].

may vary with, at most, position, $\mathbf{v}_a = (0, 0, 0)$, where a subscript ‘a’ denotes the ambient state value of the quantity to which it is attached. Our focus will be on the propagation of (acoustic) *singular surfaces* [38], specifically, shock and acceleration waves, in gases whose ambient density (i.e., ρ_a) varies exponentially; see, e.g., Refs. [14, 17], [18, § 309], and [39], as well as those cited therein, for atmospheric propagation studies in which this form of inhomogeneity arises. What is more, we shall apply our analytical and numerical tools to only the 1D versions of the acoustic models considered; specifically, those that describe (1D) propagation along the z -axis, in Section 2, and the x -axis, in Section 3.

The simulation of these singular surface phenomena through numerical methods involves the use of time-stepping schemes for partial differential equations (PDEs) that are required to use very small time step sizes, due to the coupling of low- and high-frequency components of solutions—a problem described as *stiffness*. For modeling acoustic singular surfaces in particular, high spatial resolution is required to represent these waves. This, of course, stems from the fact that all singular surface waveforms are of zero ‘thickness’, thus increasing the stiffness and shrinking the time steps even further, so that the CFL condition—a relationship between the time step size, the spatial mesh size, and the wave speed—is satisfied. This confluence of factors results in substantial computational expense, and this problem is exacerbated by increasing spatial resolution.

This dilemma can be addressed by customizing the computation of components of the solution corresponding to different frequencies, which has led to the development of Krylov subspace spectral (KSS) methods [19, 20]. KSS methods are designed to bring to variable-coefficient PDEs, defined on rectangular domains, the advantages of Fourier spectral methods for their constant-coefficient counterparts. For problems in the latter category, Fourier spectral methods effectively decouple components corresponding to different frequencies, thus allowing for efficient, scalable computation of solutions, at least for problems with smooth solutions. For variable-coefficient problems, KSS methods provide similar scalability [6] through individualized treatment of different frequencies, even though an explicit decoupling is not possible. In Ref. [21], KSS methods were applied to 1-D linear wave equations, both undamped and damped, featuring periodic media and solutions that exhibited poroacoustic shocks. In this paper, the approach from Ref. [21] is improved and generalized to handle 1-D linear or nonlinear wave equations for modeling acoustic singular surfaces.

In Section 2 of this paper we consider a hybrid initial-boundary value problem (hIBVP) that models an acoustic shock in an isothermal atmosphere under a linearized special case of Sys. (1). Although the equation of motion (EoM) that results, i.e., the 1D advected damped wave equation, has constant coefficients, the jump discontinuity that is the shock-front makes solving it via Fourier spectral methods impractical. However, it will be demonstrated that a KSS method, or more precisely, a Krylov subspace *pseudospectral* method, can solve the PDE without the need to honor the usual CFL condition, by working in both physical and Fourier space as needed; this is described in Section 4.2. This result is made possible by transforming the original hIBVP so that it is feasible to represent its solution by a Fourier sine series. In addition, the left boundary condition is homogenized in a manner that, in a sense, minimizes the effect of a newly introduced source term on the solution.

Then, in Section 3, we study the evolution of acoustic acceleration waves as they tend to finite-time blow-up, i.e., finite-time shock formation, under an inhomogeneous version of the lossless Lighthill–Westervelt equation, a weakly-nonlinear model derivable from Sys. (1). Although KSS methods were designed for linear PDEs, it will be shown that a KSS method can successfully be applied to this nonlinear PDE, again without the need to honor the usual CFL condition. While the combination of inhomogeneity and nonlinearity naturally poses additional challenges, as compared with the above-mentioned shock wave problem, it will be seen that KSS methods can be effectively applied to both problems within a common framework that can be extended to other wave propagation problems.

In Section 4, KSS based schemes are constructed for first the (linear) shock case and then the (nonlinear) acceleration wave case; see Sections 4.2 and 4.3, respectively. This section then concludes with the presentation, in the context of the respective propagation problems described above, of numerical simulations depicting snapshots in the evolution of the solution profiles exhibiting the former and latter singular surfaces. It will then be demonstrated that other time-stepping methods have difficulty resolving these singular surfaces.

And lastly, in Section 5, we record final remarks/observations and note possible follow-on investigations.

2. Linear shock waves in an isothermal atmosphere with Rayleigh dissipation

2.1. Governing system with Rayleigh dissipation

On setting $\mathbf{B} = \mathbf{B}_1 - \hat{\mu}\mathbf{v}$ and then linearizing about the ambient state, Sys. (1) becomes

$$\partial\varrho/\partial t + \nabla \cdot (\rho_a \mathbf{v}) = 0, \quad (3a)$$

$$\rho_a \partial \mathbf{v} / \partial t + \nabla \mathbf{P} = -[\nabla p_a - (\varrho + \rho_a)\mathbf{B}_1 + \hat{\mu}\rho_a \mathbf{v}], \quad (3b)$$

$$\partial \mathbf{P} / \partial t + \mathbf{v} \cdot (\nabla p_a) = c_a^2 [\partial \varrho / \partial t + \mathbf{v} \cdot (\nabla \rho_a)]. \quad (3c)$$

Here, $\mathbf{P} = p - p_a$ and $\varrho = \rho - \rho_a$, while the gas law and sound speed expressions become

$$p_a = (c_p - c_v)\rho_a \theta_a \quad (c_p, c_v := \text{const.}), \quad (4)$$

$$c_a = \sqrt{\gamma p_a / \rho_a} = \sqrt{c_p(\gamma - 1)\theta_a}, \quad (5)$$

respectively. In writing Sys. (3) we have introduced *Rayleigh's resistance law*², i.e., the term $-\hat{\mu}\mathbf{v}$, so as to prevent the shock amplitude blow-up that would otherwise afflict the solution of the hIBVP considered in the next subsection; see, e.g., Ref. [16, § 5.4]. Here, the (resistance) coefficient $\hat{\mu}(> 0)$ carries units of 1/s.

Sys. (3) can be reduced to a two-equation system as follows: First make use of the equilibrium condition

$$\nabla p_a = \rho_a \mathbf{B}_1, \quad (6)$$

by which we eliminate ∇p_a , and then use Eq. (3a) to eliminate $\partial \varrho / \partial t$ from Eqs. (3b) and (3c), after applying $\partial / \partial t$ to the former; these actions yield, after simplifying,

$$\rho_a \partial^2 \mathbf{v} / \partial t^2 + \nabla(\partial \mathbf{P} / \partial t) = -[\nabla \cdot (\rho_a \mathbf{v})]\mathbf{B}_1 - \hat{\mu}\rho_a \partial \mathbf{v} / \partial t, \quad (7a)$$

$$\partial \mathbf{P} / \partial t = -\mathbf{v} \cdot (\rho_a \mathbf{B}_1) - \rho_a c_a^2 (\nabla \cdot \mathbf{v}). \quad (7b)$$

The final step is, of course, eliminating $\partial \mathbf{P} / \partial t$ between the PDEs that comprise Sys (7); as this is easily accomplished, we omit the details and present the (vector) EoM that results, viz.:

$$\rho_a \partial^2 \mathbf{v} / \partial t^2 - \gamma \nabla(p_a \nabla \cdot \mathbf{v}) + \hat{\mu}\rho_a \partial \mathbf{v} / \partial t = \nabla[\mathbf{v} \cdot (\rho_a \mathbf{B}_1)] - [\nabla \cdot (\rho_a \mathbf{v})]\mathbf{B}_1; \quad (8)$$

compare with the EoM derived in Ref. [18, § 311], which is stated in component form, and wherein each component of the body force vector (i.e., (X, Y, Z)) is assumed constant.

2.2. Vertical propagation in a 1D, isothermal atmosphere

This case is defined by the following assumptions:

- (I) $\theta_a(z) = \theta_0$, which via Eq. (5) yields $c_a(z) = c_0$, where

$$c_0 = \sqrt{c_p(\gamma - 1)\theta_0}. \quad (9)$$

- (II) $\mathbf{B}_1 = (0, 0, -g)$, where g represents the magnitude of the (constant) acceleration due to gravity near the surface; in the case of Earth, $g \approx 9.81 \text{m/s}^2$.

- (III) 1D propagation along the z -axis; i.e., the velocity vector simplifies to $\mathbf{v} = (0, 0, w(z, t))$, while $p = p(z, t)$, $\rho = \rho(z, t)$, and $\theta = \theta(z, t)$, where the $+z$ -axis is taken to be directed vertically upward. Note also that p_a, ρ_a, θ_a , and c_a are now (at most) functions of z only.

²See, e.g., Lamb [18, p. 389], who credits this 'artifice' to Lord Rayleigh and notes, among other things, its usefulness in approximating 'small dissipative forces'. Also, Rayleigh's resistance law should not be confused with any of the numerically-motivated *artificial viscosity* methods [30] put forth since 1950.

(IV) The ‘flat Earth’ approximation (see, e.g., Ref. [22]) and the negligibility of the Earth’s rotation.

Here, $\theta_0 = (p_0/\rho_0)/(c_p - c_v)$, where $p_0, \rho_0 = \lim_{z \rightarrow 0} p_a(z), \rho_a(z)$, respectively, are both positive.

Under the first three of these assumptions, Eq. (6) reduces to

$$\frac{d\rho_a}{dz} = - \left[\frac{g}{c_v(\gamma - 1)\theta_0} \right] \rho_a; \quad (10)$$

integrating this simple ODE subject to $\rho_a(0) = \rho_0$ yields

$$\rho_a(z) = \rho_0 \exp(-z/H), \quad (11)$$

and this in turn yields, by way Eq. (4) and our assumption $\theta_a(z) = \theta_0$,

$$p_a(z) = p_0 \exp(-z/H). \quad (12)$$

Here, following convention, we have set $H = c_0^2/(\gamma g)$, where H is known as the ‘scale height of the atmosphere’ [37, p. 69].

2.3. Problem formulation and solution

In this subsection we consider the following *hybrid*³ initial-boundary value problem (hIBVP), whose EoM is the result of applying the above-listed assumptions/consequences to Eq. (8):

$$w_{tt} - c_0^2 w_{zz} + \gamma g w_z + \hat{\mu} w_t = 0, \quad (z, t) \in (0, \infty) \times (0, \infty), \quad (13a)$$

$$w(0, t) = W_0 \mathcal{H}(t) \cos(\omega t), \quad \lim_{z \rightarrow \infty} \bar{w}(z, s) = 0, \quad t, s > 0, \quad (13b)$$

$$w(z, 0) = 0, \quad w_t(z, 0) = 0, \quad z > 0. \quad (13c)$$

In hIBVP (13), which is commonly referred to in the acoustics literature as a ‘signaling problem’; $\mathcal{H}(\cdot)$ is the Heaviside unit step function; the (known) constants $W_0 (> 0)$ and $\omega (> 0)$ are the amplitude and angular frequency, respectively, of the inserted signal; and, in the present section, $\bar{w}(z, s)$ denotes the image of $w(z, t)$ in the Laplace domain, i.e.,

$$\bar{w}(z, s) = \int_0^\infty \exp(-st) w(z, t) dt \quad (s > 0), \quad (14)$$

where in this section s denotes the Laplace transform parameter; see, e.g., Ref. [5].

To determine the evolution of the shock wave modeled by this problem, we begin by applying the Laplace transform, i.e., Eq. (14), to Eq. (13a), which we observe is the (1D) advected damped wave equation [24], and the boundary condition (BC) at $z = 0$. After employing the initial conditions and simplifying, we are led to consider the subsidiary equation

$$c_0^2 \bar{w}'' - \gamma g \bar{w}' - (s^2 + \hat{\mu} s) \bar{w} = 0, \quad (15)$$

where in this section a prime denotes d/dz. Solving this ODE subject to the transformed BC, which reads $\bar{w}(0, s) = W_0 s/(s^2 + \omega^2)$, and the asymptotic condition in the Laplace domain, i.e., $\lim_{z \rightarrow \infty} \bar{w}(z, s) = 0$, yields, after some manipulation,

$$\bar{w}(z, s) = \left(\frac{W_0 s}{s^2 + \omega^2} \right) \exp[z/(2H)] \exp \left[- \left(\frac{z}{c_0} \right) \sqrt{\left(s + \frac{1}{2} \hat{\mu} \right)^2 - \chi^2} \right], \quad (16)$$

which of course is the exact solution of hIBVP (13) in the Laplace domain; here, on the assumption that $\hat{\mu} > c_0/H$ (see Section 2.4 below), we have set

$$\chi := \frac{1}{2} \sqrt{\hat{\mu}^2 - \frac{c_0^2}{H^2}}. \quad (17)$$

³See Ref. [17, Footnote 4].

Due to the relative simplicity of Eq. (16), its exact inverse can be obtained in several different ways; e.g., using a suitably extensive table of Laplace inverses and the properties of the Laplace transform. Here, we employ the results given in Ref. [5, § 90] in conjunction with the convolution theorem for Laplace transforms to show that

$$w(z, t) = W_0 \mathcal{H}(t - z/c_0) \left\{ \exp \left[- \left(\frac{\hat{\mu} - c_0/H}{2} \right) \frac{z}{c_0} \right] \cos[\omega(t - z/c_0)] + \frac{\chi z}{c_0} \int_{z/c_0}^t \frac{\exp(-\hat{\mu}\varsigma/2) \cos[\omega(t - \varsigma)] I_1 \left[\chi \sqrt{\varsigma^2 - (z/c_0)^2} \right]}{\sqrt{\varsigma^2 - (z/c_0)^2}} d\varsigma \right\}, \quad (18)$$

where in this communication $I_\nu(\cdot)$ denotes the modified Bessel function of the first kind of order ν .

2.4. Shock analysis and small-time results

An inspection of Eq. (18) reveals that w exhibits a jump discontinuity of amplitude

$$\llbracket w \rrbracket(t) = W_0 \exp \left[- \left(\frac{\hat{\mu} - \hat{\mu}_c}{2} \right) t \right], \quad (19)$$

where $\llbracket \cdot \rrbracket(t)$ is defined in Appendix A and $\hat{\mu}_c := c_0/H = \gamma g/c_0$ is a critical value of $\hat{\mu}$, across the *shock wave*⁴ $z = \Sigma(t)$, where in this section

$$\Sigma(t) = c_0 t; \quad (20)$$

here, we observe that $\Sigma(t)$ propagates to the right along the z -axis with speed

$$\frac{d\Sigma(t)}{dt} = c_0. \quad (21)$$

From Eq. (19) it is clear that we must take $\hat{\mu} > \hat{\mu}_c$ if we are to have $\llbracket w \rrbracket(t) \rightarrow 0$ as $t \rightarrow \infty$. Eq. (19) also makes clear that $\llbracket w \rrbracket(t)$ is independent of ω ; see Eq. (23) below.

The transient nature of $\llbracket w \rrbracket(t)$, which follows from our assumption $\hat{\mu} > \hat{\mu}_c$, and the complicated nature of Eq. (18) motivate us to seek a simpler, approximate expression for the latter—one that is valid for small- t . To this end, we turn to Ref. [5, §§ 123, 124] and expand Eq. (16) for large- s ; this yields, after simplifying,

$$\bar{w}(z, s) \sim W_0 s^{-1} \exp(-sz/c_0) \exp \left[- \left(\hat{\mu} - \frac{c_0}{H} \right) \frac{z}{2c_0} \right] \left\{ 1 + \left(\frac{\hat{\mu}^2 - c_0^2/H^2}{8c_0} \right) \frac{z}{s} + \left[\frac{1}{2} \left(\frac{\hat{\mu}^2 - c_0^2/H^2}{8} \right)^2 \left(\frac{z}{c_0} \right)^2 - \frac{\hat{\mu}}{2} \left(\frac{\hat{\mu}^2 - c_0^2/H^2}{8} \right) \left(\frac{z}{c_0} \right) - \omega^2 \right] \frac{1}{s^2} + \mathcal{O}(s^{-3}) \right\} \quad (s \rightarrow \infty). \quad (22)$$

Inverting term-by-term using a standard table of inverses [5], we find that

$$w(z, t) \approx W_0 \mathcal{H}(t - z/c_0) \exp \left[- \left(\frac{\hat{\mu} - \hat{\mu}_c}{2} \right) \frac{z}{c_0} \right] \left\{ 1 + \left(\frac{\hat{\mu}^2 - \hat{\mu}_c^2}{8} \right) \left(\frac{z}{c_0} \right) (t - z/c_0) + \frac{1}{2} \left[\frac{1}{2} \left(\frac{\hat{\mu}^2 - \hat{\mu}_c^2}{8} \right)^2 \left(\frac{z}{c_0} \right)^2 - \frac{\hat{\mu}}{2} \left(\frac{\hat{\mu}^2 - \hat{\mu}_c^2}{8} \right) \left(\frac{z}{c_0} \right) - \omega^2 \right] (t - z/c_0)^2 \right\}, \quad (23)$$

where terms of $\mathcal{O}[(t - z/c_0)^3]$ have been neglected. It should be noted that while Eq. (23) can be expected to prove accurate at, and in the nearby-neighborhood of, $z = \Sigma(t)$ for all $t > 0$, its usefulness as a global approximation to w is limited to sufficiently small values of t .

We conclude this subsection with the following observations: (i) Note that $\hat{\mu}_c = 1/t_H$, where $\Sigma(t_H) = H$; i.e., the critical value of $\hat{\mu}$ is the reciprocal of the time taken by Σ to propagate from $z = 0$ to $z = H$. (ii) For t sufficiently small, the impact of ω is of only second order. And (iii), Eq. (19) could have also been obtained directly from Eq. (22) via the application of the theorem in Ref. [3, § 4].

⁴As defined in Appendix A.

2.5. Large-time asymptotic results

Using the properties of the Laplace transform detailed in Ref. [5, § 126], it is not difficult to establish that, to lowest order, the large- t behavior of Eq. (18) is described by

$$w(z, t) \sim W_0 \exp \left[- \left(\frac{\sigma - \hat{\mu}_c}{2} \right) \frac{z}{c_0} \right] \cos \left[\omega t - \frac{1}{2} (\varkappa / c_0) z \right] \quad (t \rightarrow \infty), \quad (24)$$

where

$$\sigma = \sqrt{\frac{\hat{\mu}_c^2 - 4\omega^2 + \sqrt{(\hat{\mu}_c^2 - 4\omega^2)^2 + 16(\hat{\mu}\omega)^2}}{2}} \quad \text{and} \quad \varkappa = \sqrt{\frac{-\hat{\mu}_c^2 + 4\omega^2 + \sqrt{(\hat{\mu}_c^2 - 4\omega^2)^2 + 16(\hat{\mu}\omega)^2}}{2}}. \quad (25)$$

It can be shown that $\sigma \in (\hat{\mu}_c, \hat{\mu})$ for all $\omega > 0$, where we recall our assumption $\hat{\mu}_c < \hat{\mu}$; thus, provided $\hat{\mu}_c < \hat{\mu}$ holds, $w(z, t) \rightarrow 0$, as $z \rightarrow \infty$, under Eq. (18).

Also noteworthy is the fact that Eq. (24) admits the high-frequency simplification:

$$w(z, t) \sim W_0 \exp \left[- \left(\frac{\hat{\mu} - \hat{\mu}_c}{2} + \mathcal{O}(\omega^{-2}) \right) \frac{z}{c_0} \right] \cos \left[\omega t - \omega \left(1 + \frac{\hat{\mu}^2 - \hat{\mu}_c^2}{8\omega^2} + \mathcal{O}(\omega^{-4}) \right) \frac{z}{c_0} \right] \quad (t \rightarrow \infty), \quad (26)$$

a waveform with phase velocity

$$V_{\text{ph}} \sim c_0 \left[1 - \frac{\hat{\mu}^2 - \hat{\mu}_c^2}{8\omega^2} + \mathcal{O}(\omega^{-4}) \right] \quad (\omega \rightarrow \infty). \quad (27)$$

Eq. (27) indicates that, although attenuated, our waveform exhibits *dispersion-free* propagation in the limit $\omega \rightarrow \infty$.

We conclude this subsection by asking the reader to compare Eq. (26) with the large- t expression derived in Ref. [23, (9) § 4-17] for a variant of hBVP (13); therein, among other differences, ‘ β ’ plays the role of $\frac{1}{2}\hat{\mu}$, where ‘ β ’ should be regarded as though it were independent of ‘ ω ’, and $\hat{\mu}_c := 0$.

3. Nonlinear effects: Acceleration waves under a variable-coefficient Lighthill–Westervelt equation

Assuming $p_a(\mathbf{x}) \equiv p_0$, the lossless version of the inhomogeneous Lighthill–Westervelt equation (ihLWE) can be expressed as [31, Eq. (2.55)]

$$\varphi_{tt} - c_a^2(\mathbf{x}) \nabla^2 \varphi + \rho_a^{-1}(\mathbf{x}) c_a^2(\mathbf{x}) \{ [\nabla \rho_a(\mathbf{x})] \cdot \nabla \varphi \} = \beta \rho_a^{-1}(\mathbf{x}) c_a^{-2}(\mathbf{x}) \partial_{tt}(\varphi^2); \quad (28)$$

see also Ref. [36, Eq. (2)], taking note of the fact that ‘ κ_0 ’ therein is equal to $1/(\gamma p_0)$ in the present section. In Eq. (28), $\varphi(\mathbf{x}, t) = p(\mathbf{x}, t) - p_0$ denotes the acoustic pressure; β , the coefficient of nonlinearity, is given by $\beta = (\gamma + 1)/2$ in the case of perfect gases; and in this communication we let

$$\partial_{\zeta}, \partial_{\zeta\zeta} := \partial^{1,2} / \partial \zeta^{1,2}, \quad (29)$$

respectively. This weakly-nonlinear EoM is readily derived from Sys. (1) after setting $\mathbf{B} = (0, 0, 0)$, which follows from our assumptions $p_a(\mathbf{x}) \equiv p_0$ and $\mathbf{v}_a = (0, 0, 0)$, and invoking the *finite-amplitude approximation scheme* (FAAS); see, e.g., Ref. [31, § 2.1]⁵. In carrying out the analysis in this section, we will make use of the fact that Eq. (28) can also be expressed as

$$c_a^2(\mathbf{x}) \nabla^2 \Phi - \Phi_{tt} + c_a^2(\mathbf{x}) \nabla \cdot \{ [\rho_a^{-1}(\mathbf{x}) \nabla \rho_a(\mathbf{x})] \Phi \} = \beta c_a^{-2}(\mathbf{x}) \partial_{tt}[(\Phi_t)^2]; \quad (30)$$

here, $\mathbf{v} = \nabla \Phi$, where $\Phi = \Phi(\mathbf{x}, t)$ is the scalar velocity potential, and we note that φ, Φ are related via

$$\varphi = -\rho_a(\mathbf{x}) \Phi_t + \text{h.o.t.} \quad (31)$$

⁵The system stated in Ref. [31, p. 3] reduces to a form equivalent to Sys. (1) on setting $\kappa, \mu, K, q = 0$, and replacing \mathbf{F} with $\rho \mathbf{B}$, in the former.

In the case of 1D propagation along the x -axis, $\mathbf{v} = (u(x, t), 0, 0)$, where now $u(x, t) = \Phi_x(x, t)$, and the acoustic pressure simplifies to $\varphi(x, t) = p(x, t) - p_0$, while ρ_a and c_a become functions of (at most) x ; consequently, Eqs. (28) and (30) are reduced to

$$\varphi_{tt} - c_a^2(x)\varphi_{xx} + c_a^2(x)[\rho'_a(x)/\rho_a(x)]\varphi_x = \beta\rho_a^{-1}(x)c_a^{-2}(x)\partial_{tt}(\varphi^2), \quad (32)$$

$$c_a^2(x)\Phi_{xx} - \Phi_{tt} + c_a^2(x)\partial_x\{[\rho'_a(x)/\rho_a(x)]\Phi\} = \beta c_a^{-2}(x)\partial_t[(\Phi_t)^2], \quad (33)$$

respectively, where in this section a prime denotes d/dx .

If we now assume the ambient density of the gas exhibits the following *exponential* profile:

$$\rho_a(x) = \rho_0 \exp(\alpha x/\ell), \quad (34)$$

then, by Eq. (5) and our earlier assumption $p_a(x) = p_0$, it follows that $c_a(x) = \hat{c}_a(x)$, where

$$\hat{c}_a(x) = c_0 \exp[-\alpha x/(2\ell)]. \quad (35)$$

Here, $c_0 = \sqrt{\gamma p_0/\rho_0}$, as in the previous section; $\alpha (\neq 0)$ is a free (dimensionless) parameter; and $\ell (> 0)$ is the length of the propagation domain. On making these substitutions and simplifying, Eqs. (32) and (33) reduce to

$$\varphi_{tt} - \hat{c}_a^2(x)\varphi_{xx} + (\alpha/\ell)\hat{c}_a^2(x)\varphi_x = p_0^{-1}(\beta/\gamma)\partial_{tt}(\varphi^2), \quad (36)$$

$$\hat{c}_a^2(x)\Phi_{xx} - \Phi_{tt} + (\alpha/\ell)\hat{c}_a^2(x)\Phi_x = \beta\hat{c}_a^{-2}(x)\partial_t[(\Phi_t)^2], \quad (37)$$

respectively.

We seek to analytically investigate, and later numerically solve, Eq. (36) subject to the following BCs and ICs:

$$\varphi(0, t) = p_{\text{pk}}\mathcal{H}(t)\sin(\omega t), \quad \varphi(\ell, t) = 0 \quad (0 < t < t_f); \quad \varphi(x, 0) = 0, \quad \varphi_t(x, 0) = 0 \quad (0 < x < \ell), \quad (38)$$

where, adopting the notation of Ref. [28, § 1-8], the parameters $p_{\text{pk}} (> 0)$ and $\omega (> 0)$ denote the peak pressure (or amplitude) and angular frequency, respectively, of the inserted signal. Moreover, we let $t_f (> 0)$ represent the final (i.e., largest) instant of time at which we seek to compute φ , and we recall that $\mathcal{H}(\cdot)$ denotes the Heaviside unit step function.

To this end, we introduce the following dimensionless variables:

$$P = \varphi/p_{\text{pk}}, \quad X = x/\ell, \quad T = (c_0/\ell)t, \quad \mathbf{U} = u/u_c, \quad (39)$$

where $u_c (> 0)$ denotes a characteristic value of the velocity field, and consider the following (dimensionless) signaling IBVP involving the ihLWE:

$$(1 - 2\epsilon\hat{\beta}P)P_{TT} - V_a^2(X)P_{XX} + \alpha V_a^2(X)P_X = 2\epsilon\hat{\beta}(P_T)^2, \quad (X, T) \in (0, 1) \times (0, T_f), \quad (40a)$$

$$P(0, T) = \mathcal{H}(T)\sin(\pi T), \quad P(1, T) = 0, \quad T \in (0, T_f), \quad (40b)$$

$$P(X, 0) = 0, \quad P_T(X, 0) = 0, \quad X \in (0, 1). \quad (40c)$$

In IBVP (40), $\epsilon = p_{\text{pk}}/p_0$, where $\epsilon \ll 1$ is assumed in accordance with the FAAS; we have set

$$\hat{\beta} := \beta/\gamma = (1 + 1/\gamma)/2, \quad (41)$$

where $\hat{\beta} \in [4/5, 1)$; the dimensionless form of $\hat{c}_a^2(x)$ is

$$V_a^2(X) = \exp(-\alpha X); \quad (42)$$

we have taken the dimensionless signal frequency equal to π ; T_f , the dimensionless version of t_f , is given by

$$T_f = \begin{cases} \begin{cases} T_1, & \alpha \in (-\infty, 0) \cup (0, \alpha^*], \\ T_\infty, & \alpha > \alpha^*, \end{cases} & \epsilon \in (0, \epsilon^*), \\ \begin{cases} T_1, & \alpha < 0, \\ T_\infty, & \alpha > 0, \end{cases} & \epsilon = \epsilon^*, \quad \alpha \neq 0, \\ \begin{cases} T_1, & \alpha < -|\alpha^*|, \\ T_\infty, & \alpha \in [-|\alpha^*|, 0) \cup (0, +\infty), \end{cases} & \epsilon > \epsilon^*, \end{cases} \quad (43)$$

where we have set

$$\epsilon^\bullet := 1/(\pi\hat{\beta}); \quad (44)$$

and T_1 , T_∞ , and α^\bullet are defined below in Eqs. (52), (53), and (54), respectively.

Now making use of Eq. (31) and the relation $u(x, t) = \Phi_x(x, t)$, it is not difficult to decompose Eq. (37) into the (kinematic-like) system

$$\epsilon(1 - 2\epsilon\hat{\beta}P)P_T + \gamma\text{Ma}U_X = -(\gamma\alpha\text{Ma})U, \quad (45a)$$

$$\gamma\text{Ma}\exp(\alpha X)U_T + \epsilon P_X = \epsilon\alpha P, \quad (45b)$$

which we have expressed in terms of the dimensionless variables defined in Eq. (39). In Sys. (45), all h.o.t. terms have been neglected, in accordance with the FAAS, and $\text{Ma} = u_c/c_0$ is the Mach number, where, also based on the FAAS, $\text{Ma} \ll 1$ is assumed.

In the case of IBVP (40), it is readily established, by first taking jumps of Sys. (45), and then applying the tools of singular surface theory (see Appendix A) to the resulting jump equations, that the amplitudes of the jumps in the first derivatives of P , i.e., the acceleration wave amplitudes, are given by

$$\llbracket P_T \rrbracket(T) = \frac{3\alpha\pi\sqrt{1 + \alpha T/2}}{(3\alpha + 4\pi\epsilon\hat{\beta}) - 4\pi\epsilon\hat{\beta}(1 + \alpha T/2)^{3/2}}, \quad (46)$$

$$\llbracket P_X \rrbracket(T) = \frac{-3\alpha\pi(1 + \alpha T/2)^{3/2}}{(3\alpha + 4\pi\epsilon\hat{\beta}) - 4\pi\epsilon\hat{\beta}(1 + \alpha T/2)^{3/2}}. \quad (47)$$

Moreover, both the former and latter occur across the the (planar) surface $X = \mathcal{V}(T)$, where

$$\mathcal{V}(T) = 2\alpha^{-1} \ln\left(1 + \frac{1}{2}\alpha T\right). \quad (48)$$

Here, $X = \mathcal{V}(T)$ is the equation of the *acceleration wave-front* associated with IBVP (40); i.e., $\mathcal{V}(T)$ is the dimensionless form of the expression for $\Sigma(t)$ in the present section (again, see Appendix A).

It should be noted that Eq. (46) was determined first; Eq. (47) then followed from the former via Eq. (A.3), which in the present setting assumes the form:

$$\mathcal{V}(T)\llbracket P_X \rrbracket(T) = -\llbracket P_T \rrbracket(T). \quad (49)$$

Here, $\mathcal{V}(T) = d\mathcal{V}(T)/dT$ is easily shown to be given by

$$\mathcal{V}(T) = \frac{1}{1 + \frac{1}{2}\alpha T}, \quad (50)$$

where $\mathcal{V}(T)(> 0)$ is the velocity at which $\mathcal{V}(T)$ propagates (to the right) along the X -axis. Also, Eq. (48) was obtained by integrating the following ODE subject to the initial condition $\mathcal{V}(0) = 0$:

$$(d\mathcal{V}(T)/dT)^2 = V_a^2(\mathcal{V}(T)), \quad (51)$$

where we observe that $\mathcal{V}(T_1) = 1$; here, $T_1(> 0)$, which is given by

$$T_1 := \frac{2[\exp(\alpha/2) - 1]}{\alpha}, \quad (52)$$

is the (dimensionless) time at which $X = \mathcal{V}(T)$ makes its *initial* arrival at the right boundary (i.e., $X = 1$).

Of particular interest to us, however, is the following: An inspection of Eqs. (46) and (47) reveals that both amplitude expressions are capable of exhibiting finite-time shock formation; specifically, $|\llbracket P_T \rrbracket(T_\infty)| = |\llbracket P_X \rrbracket(T_\infty)| = \infty$, where the (common) blow-up time is given by

$$T_\infty = -\frac{2}{\alpha} \left[1 - \left(1 + \frac{3\alpha}{4\pi\epsilon\hat{\beta}} \right)^{2/3} \right]. \quad (53)$$

To simplify our analysis of this phenomenon, we henceforth assume that $\alpha = \alpha^\bullet$; here, recalling Eqs. (43) and (44), we record the expressions

$$\alpha^\bullet := -\frac{4}{3} \begin{cases} \epsilon \hat{\beta} \pi + \mathbb{W}_{-1}[-\epsilon \hat{\beta} \pi \exp(-\epsilon \hat{\beta} \pi)], & \epsilon \in (0, \epsilon^\bullet), \\ \epsilon \hat{\beta} \pi + \mathbb{W}_0[-\epsilon \hat{\beta} \pi \exp(-\epsilon \hat{\beta} \pi)], & \epsilon > \epsilon^\bullet, \end{cases} \quad (54)$$

which were derived by setting the right-hand side of Eq. (52) equal to the right-hand side of Eq. (53) and then solving for α . In Eq. (54), wherein we have *implicitly* imposed the restriction $\epsilon \neq \epsilon^\bullet$ to ensure that $\alpha^\bullet \neq 0$, we have used $\mathbb{W}_{-1,0}(\cdot)$ to denote the ‘negative one’ and ‘principal’ branches, respectively, of the Lambert W -function [7].

Thus, in what follows,

$$T_f = T_\infty \Big|_{\alpha=\alpha^\bullet} = T_1 \Big|_{\alpha=\alpha^\bullet}; \quad (55)$$

recall Eqs. (43). A consequence of this equality is, of course, that

$$\mathcal{V}(T_\infty) \Big|_{\alpha=\alpha^\bullet} = 1. \quad (56)$$

For $\alpha = \alpha^\bullet$, then, Eq. (56) indicates that shock formation occurs the *instant* our acceleration wave-front $X = \mathcal{V}(T)$ arrives at the right boundary; here, we observe that $\alpha^\bullet > 0$ (resp. $\alpha^\bullet < 0$) for $\epsilon \in (0, \epsilon^\bullet)$ (resp. $\epsilon > \epsilon^\bullet$).

Because we have selected $\alpha = \alpha^\bullet$, and $\alpha^\bullet > \alpha_{\text{crit}}$, an inequality which is easily verified, it follows that $T_\infty \in \mathbb{R}^+$; here,

$$\alpha_{\text{crit}} = -\frac{4\pi\epsilon\hat{\beta}}{3}, \quad (57)$$

where we observe that $\alpha = \alpha_{\text{crit}}$ (resp. $\alpha < \alpha_{\text{crit}}$) implies that $T_\infty = T_{\text{BD}}$ (resp. $T_\infty \in \mathbb{C}$). What we denote by $T_{\text{BD}}(> 0)$ is the value of T at which the *breakdown* of the $\alpha < 0$ case of the ihLWE occurs; it is given by

$$T_{\text{BD}} = \frac{2}{|\alpha|} \quad (\alpha < 0), \quad (58)$$

and by ‘breakdown’ we mean $\mathcal{V}(T), \mathcal{Y}(T) \rightarrow \infty$ as $T \rightarrow T_{\text{BD}}$, which we stress is a possibility only when $\alpha < 0$. We hasten to point out, however, that this breakdown *cannot* occur under the present formulation/assumptions because the present analysis is limited (at most) to $T \in (0, T_f)$, but $T_f = T_1 = T_\infty < T_{\text{BD}}$ when $\alpha = \alpha^\bullet$ is taken.

We conclude this section by recording the following limits, which correspond to the case $\rho_a(x) \equiv \rho_0$:

$$\lim_{\alpha \rightarrow 0} \llbracket P_T \rrbracket(T) = -\lim_{\alpha \rightarrow 0} \llbracket P_X \rrbracket(T) = \frac{\pi}{1 - \epsilon \hat{\beta} \pi T} \quad \implies \quad \lim_{\alpha \rightarrow 0} T_\infty = \gamma / (\epsilon \hat{\beta} \pi); \quad (59)$$

these expression should be compared with their counterparts in Ref. [15], wherein a different non-dimensionalization scheme was employed.

4. Numerical scheme construction

4.1. Overview of KSS methods

Before providing the details of the proposed numerical methods that will be applied to IBVP (13) and IBVP (40), we will describe the Krylov subspace spectral (KSS) methodology in the context of its application to a simpler problem. We consider the IBVP

$$u_{tt} + Lu = 0, \quad 0 < x < 1, \quad t > 0, \quad (60a)$$

$$u(0, t) = 0, \quad u(1, t) = 0, \quad t > 0, \quad (60b)$$

$$u(x, 0) = f(x), \quad u_t(x, 0) = g(x), \quad 0 < x < 1, \quad (60c)$$

where the differential operator L is defined by

$$Lu = -\kappa_1 u_{xx} + q(x)u. \quad (61)$$

We discretize on a uniform N -point grid $\{x_i\}_{i=1}^N$, where $x_i = i\Delta x$ and $\Delta x = 1/(N+1)$. This yields the system of ODEs

$$\mathbf{u}_N''(t) = -L_N \mathbf{u}_N(t), \quad t > 0, \quad (62a)$$

$$\mathbf{u}_N(0) = \mathbf{f}_N, \quad \mathbf{u}_N'(0) = \mathbf{g}_N, \quad (62b)$$

where L_N is a $N \times N$ matrix obtained via spatial discretization of L , say, by finite differences, and \mathbf{f}_N and \mathbf{g}_N are discretizations of $f(x)$ and $g(x)$, respectively. Moreover, in this section a prime indicates the derivative of a function of a single (real) variable. This system of ODEs has the exact solution

$$\mathbf{u}_N(t + \Delta t) = F_{11}(L_N, \Delta t) \mathbf{u}_N(t) + F_{12}(L_N, \Delta t) \mathbf{u}_N'(t), \quad (63a)$$

$$\mathbf{u}_N'(t + \Delta t) = F_{21}(L_N, \Delta t) \mathbf{u}_N(t) + F_{22}(L_N, \Delta t) \mathbf{u}_N'(t), \quad (63b)$$

where the matrix functions $F_{ij}(L_N, \Delta t)$, $i, j = 1, 2$, are given by

$$F_{11}(L_N, \Delta t) = F_{22}(L_N, \Delta t) = \cos(L_N^{1/2} \Delta t), \quad F_{12}(L_N, \Delta t) = L_N^{-1/2} \sin(L_N^{1/2} \Delta t), \quad F_{21}(L_N, \Delta t) = -L_N^{1/2} \sin(L_N^{1/2} \Delta t). \quad (64)$$

However, for large values of N , it is not practical to compute these matrix functions directly.

Let \mathbf{u}_N^n represent an approximate solution of Sys. (62) at time t_n . A KSS method computes \mathbf{u}_N^n as follows:

$$\mathbf{u}_N^{n+1} = \tilde{F}_{11}(L_N, \Delta t) \mathbf{u}_N^n + \tilde{F}_{12}(L_N, \Delta t) [\mathbf{u}_N']^n, \quad (65a)$$

$$[\mathbf{u}_N']^{n+1} = \tilde{F}_{21}(L_N, \Delta t) \mathbf{u}_N^n + \tilde{F}_{22}(L_N, \Delta t) [\mathbf{u}_N']^n. \quad (65b)$$

In this paper, we will focus exclusively on a KSS method for systems of this form, with the addition of source terms, that are second-order accurate in time; higher-order methods are described in Ref. [20] for wave propagation problems, and in Refs. [6, 19] for other types of PDEs.

Let S_N be the matrix of the N -point discrete sine transform. For $i, j = 1, 2$, $\tilde{F}_{ij}(L_N, \Delta t)$ is an approximation of $F_{ij}(L_N, \Delta t)$ that has the form

$$\tilde{F}_{ij}(L_N, \Delta t) = S_N^{-1} \left[B^{ij}(\Delta t) S_N + M^{ij}(\Delta t) S_N L_N \right], \quad (66)$$

where $B^{ij}(\Delta t)$ and $M^{ij}(\Delta t)$ are diagonal matrices. For $k = 1, 2, \dots, N$, the k th diagonal entries $[B^{ij}(\Delta t)]_{kk}$ and $[M^{ij}(\Delta t)]_{kk}$ are the y -intercept and slope, respectively, of the function $\mathcal{P}_{ij,k}(\lambda, \Delta t)$, that, for fixed Δt , is a linear function that interpolates $F_{ij}(\lambda, \Delta t)$ at frequency-dependent interpolation points $\lambda_{1,k}, \lambda_{2,k}$.

It remains to determine the interpolation points $\lambda_{1,k}, \lambda_{2,k}$ for each wave number k . In this paper, the matrix L_N is a finite difference discretization of the differential operator L in which the second derivative is approximated by a centered difference. Therefore, as in Ref. [29], we choose

$$\lambda_{1,k} = 0, \quad \lambda_{2,k} = \kappa_1(2 - 2 \cos(\pi k \Delta x)) / (\Delta x)^2 + \text{avg}(q), \quad (67)$$

where $\text{avg}(q)$ denotes the average value of the coefficient $q(x)$ on $(0, 1)$. That is, $\lambda_{2,k}$ is an approximate eigenvalue of L_N .

This approach to solving IBVP (60) is second-order accurate in time and has spectral accuracy in space; see Ref. [29] for a convergence analysis, including a proof that the method is unconditionally stable for a similar problem, in which periodic boundary conditions were imposed. This kind of stability normally occurs only in time-stepping methods that are either implicit, or involve some kind of iteration such as Krylov projection [13].

Krylov subspace methods for approximating matrix function-vector products of the form $\varphi(A)\mathbf{b}$ for a matrix A and vector \mathbf{b} , such as those described in Ref. [13] in the case of the matrix exponential, generate a Krylov subspace of sufficient dimension to ensure the desired accuracy of the approximation. When such methods are used to solve stiff systems of ODEs derived from PDEs, the required Krylov subspace dimension can grow substantially when increasing the time step, or, depending on the PDE, the number of grid points in the spatial discretization [6].

By contrast, in a KSS method, the Krylov subspace dimension is independent of the time step or spatial grid size; rather, it is determined solely by the order of temporal accuracy. For example, in the KSS method defined by Eq. (66), for each approximation of a matrix function-vector product, only one matrix-vector multiplication (excluding multiplication by diagonal matrices, which of course is implemented as component-wise multiplication of vectors),

at most two Fourier transforms, and one inverse Fourier transform are required. As such, KSS methods realize stability and scalability [6] superior to that of similar time-stepping methods, through the use of frequency-dependent approximations of the solution operator of the PDE. In the remainder of this section, we discuss how a second-order KSS method can be applied to the problems presented in this paper.

4.2. Shock case

To solve hIBVP (13) numerically, we first modify the problem so that it is defined on a bounded domain $(0, \ell)$. That is, we consider

$$w_{tt} - c_0^2 w_{zz} + \gamma g w_z + \hat{\mu} w_t = 0, \quad 0 < z < \ell, \quad t > 0, \quad (68a)$$

$$w(z, 0) = w_t(z, 0) = 0, \quad (68b)$$

$$w(0, t) = \mathcal{H}(t) \cos(\omega t), \quad (68c)$$

where, for the moment, we have set $W_0 = 1$. Since the boundary condition causes a shock wave that is entering from the left, the solution will be zero to the right of the wave front. Therefore, we impose the right-end boundary condition $w(\ell, t) = 0$. Due to the Dirichlet boundary conditions, we use a Fourier sine series. Thus, we must transform the problem to eliminate first derivative terms and homogenize the the left boundary condition.

4.2.1. Transforming the PDE

We first simplify Eq. (68a), which we note appears (in IBVP (68)) unchanged from its role as the EoM in hIBVP (13a), by introducing a differential operator L , defined by

$$Lw = -a_2 w_{zz} + a_1 w_z,$$

where $a_2 = c_0^2$ and $a_1 = \gamma g$; in terms of L , then, Eq. (68a) becomes

$$w_{tt} = -Lw - \hat{\mu} w_t. \quad (69)$$

Proceeding as suggested in Ref. [9], by defining

$$w(z, t) = \psi(z, t) \tilde{w}(z, t), \quad \psi(z) = \exp\left[\left(\frac{a_1}{2a_2}\right)z\right],$$

we obtain the equivalent PDE

$$\tilde{w}_{tt} = -\tilde{L}\tilde{w} - \hat{\mu}\tilde{w}_t,$$

where

$$\tilde{L}\tilde{w} = -a_2 \tilde{w}_{zz} + a_0 \tilde{w}, \quad a_0 = \frac{a_1^2}{4a_2}.$$

4.2.2. Homogenizing the boundary conditions

We now transform the hIBVP into an equivalent problem with homogeneous boundary conditions,

$$u_{tt} = -\tilde{L}u - \hat{\mu}u_t - G(z, t), \quad (70a)$$

$$u(0, t) = 0, \quad u(\ell, t) = 0, \quad (70b)$$

$$u(z, 0) = -F(z, 0), \quad u_t(z, 0) = -F_t(z, 0), \quad (70c)$$

where

$$G(z, t) = F_{tt} + a_2 F_{zz} + a_0 F + \hat{\mu} F_t$$

is the source term introduced by transforming the left boundary condition. We use an approach to homogenization of boundary conditions described in Ref. [9], except that we also require that the source term $G(z, t)$ satisfies

$$G(0, t) = 0, \quad (71a)$$

$$G(z, t) = 0, \quad z \geq \tilde{\ell}, \quad (71b)$$

for some $\tilde{\ell} < \ell$. We choose $\tilde{\ell} = 80\Delta z$ for the implementation, where Δz is the spatial grid mesh, but numerical experimentation indicates that the performance of the numerical method is not sensitive to the choice of $\tilde{\ell}$. A similar approach to homogenization was used in Ref. [21], except that in this case, we require that $G(z, t)$ vanishes on most of the spatial domain, instead of only at the right endpoint. This mitigates numerical artifacts, caused by truncation error, in the solution to the right of the wavefront.

The solution of Eq. (70) is then written as

$$u(z, t) = \tilde{w}(z, t) - F(z, t),$$

where

$$F(z, t) = \begin{cases} f_0(t) + f_1(t)z + f_2(t)z^2 + f_3(t)z^3 + f_4(t)z^4 & 0 \leq z \leq \tilde{\ell} \\ 0 & \tilde{\ell} < z \leq \ell. \end{cases}$$

satisfies not only the original boundary conditions, but also belongs to $C^2([0, \ell])$. That is, we require

$$F(0, t) = \cos(\omega t), \quad (72a)$$

$$F(\tilde{\ell}, t) = 0, \quad (72b)$$

$$F_z(\tilde{\ell}, t) = 0, \quad (72c)$$

$$F_{zz}(\tilde{\ell}, t) = 0. \quad (72d)$$

The smoothness requirements on F , an additional modification of the homogenization scheme from Ref. [21], are imposed to increase the decay rate of Fourier coefficients of the solution and thus reduce high-frequency oscillations.

From condition (71a), we obtain

$$\begin{aligned} f_2(t) &= \frac{1}{2a_2} (f_0''(t) + a_0 f_0(t) + \hat{\mu} f_0'(t)) \\ &= -\frac{\omega^2}{2a_2} \cos(\omega t) + \frac{a_0}{2a_2} \cos(\omega t) - \frac{\hat{\mu}\omega}{2a_2} \sin(\omega t). \end{aligned}$$

We then use the conditions (71b), (72b), and (72c) in a 3×3 system of linear equations to obtain $f_1(t)$, $f_3(t)$, and $f_4(t)$. Condition (72d) is also satisfied as a result.

4.2.3. Approximate solution operator

Now, we express the solution at time t_{n+1} in terms of the solution at time $t_n = n\Delta t$. We will work with a PDE of the form

$$u_{tt} = -\tilde{L}u + b(z, t_n), \quad (73)$$

where \tilde{L} is a positive definite second-order spatial differential operator, and $b(z, t_n) = -\hat{\mu}u_t(z, t_n) - G(z, t_n)$ is treated as a source term, as a first-order approximation of Eq. (70a). We then rewrite Eq. (73) as a first-order system

$$\begin{bmatrix} u \\ u_t \end{bmatrix}_t = J \begin{bmatrix} u \\ u_t \end{bmatrix} + \begin{bmatrix} 0 \\ b \end{bmatrix}, \quad J = \begin{bmatrix} 0 & \mathbb{I} \\ -\tilde{L} & 0 \end{bmatrix}, \quad (74)$$

where we use \mathbb{I} to denote the identity operator. If we define

$$\mathbf{r} = \begin{bmatrix} u \\ u_t \end{bmatrix}, \quad \mathbf{c}_n = \begin{bmatrix} 0 \\ b(z, t_n) \end{bmatrix},$$

then, as in Ref. [27], we can express the solution of Sys. (74) as

$$\mathbf{r}(t_{n+1}) = \phi_0(J\Delta t)\mathbf{r}(t_n) + \Delta t\phi_1(J\Delta t)\mathbf{c}_n, \quad (75)$$

where

$$\phi_0(Jt) = \begin{bmatrix} \cos(\tilde{L}^{1/2}t) & \tilde{L}^{-1/2} \sin(\tilde{L}^{1/2}t) \\ -\tilde{L}^{1/2} \sin(\tilde{L}^{1/2}t) & \cos(\tilde{L}^{1/2}t) \end{bmatrix} \quad (76)$$

and

$$t\phi_1(Jt) = \begin{bmatrix} \tilde{L}^{-1/2} \sin(\tilde{L}^{1/2}t) & \tilde{L}^{-1} - \tilde{L}^{-1} \cos(\tilde{L}^{1/2}t) \\ \cos(\tilde{L}^{1/2}t) - \mathbb{I} & \tilde{L}^{-1/2} \sin(\tilde{L}^{1/2}t) \end{bmatrix}. \quad (77)$$

What remains is to apply spatial discretization to Eq. (75), and then compute the various matrix function-vector products indicated by Eqs. (76) and (77).

4.2.4. Numerical solution via KSS

The computed solution (Eq. (75)) of the PDE involves approximating functions of a matrix \tilde{L}_N , that is identified with a differential operator \tilde{L} that \tilde{L}_N discretizes through centered differencing. The operator \tilde{L} in this case will be the result of the transformation described previously,

$$\tilde{L}u = -a_2u_{zz} + a_0u.$$

To approximate $f(\tilde{L}_N)\mathbf{u}_N$ for a given function f and vector \mathbf{u}_N using a second-order KSS approximation, as in Sys. (65), we first select frequency-dependent interpolation points as in Eq. (67),

$$\lambda_{1,k} = 0, \quad \lambda_{2,k} = a_2(2 - 2\cos(\omega_k\Delta z))/(\Delta z)^2 + a_0, \quad (78)$$

where $\omega_k = \pi k/\ell$, for $k = 1, 2, \dots, N$, and $\lambda_{2,k}$ is an eigenvalue of \tilde{L}_N . Based on Eq. (66), the approximation is then

$$f(\tilde{L}_N)\mathbf{u}_N \approx S_N^{-1}[B_k S_N \mathbf{u}_N + M_k S_N \tilde{L}_N \mathbf{u}_N], \quad (79)$$

where B_k and M_k are diagonal matrices, the diagonal entries of which are the y -intercepts and slopes, respectively, of the linear approximation of f for each frequency ω_k with interpolation points from Eq. (78). The operators S_N and S_N^{-1} represent the N -point discrete sine transform and its inverse, respectively.

It is worth noting that because the operator \tilde{L} has constant coefficients, Eq. (79) can be simplified to

$$f(\tilde{L}_N)\mathbf{u}_N \approx S_N^{-1}f(\Lambda_2)S_N \mathbf{u}_N, \quad (80)$$

where Λ_2 is a diagonal matrix with diagonal entries $\lambda_{2,k}$, $k = 1, 2, \dots, N$. In this case, the KSS method reduces to a Fourier spectral method. However, in numerical experiments, it was found that this simplified formula led to high-frequency oscillations in the solution, known as Gibbs' phenomenon, brought on by substantial accumulation of round-off error, whereas using Eq. (79) as written did not. As will be illustrated later in this section, even with enough regularization to keep the solution bounded, using a Fourier spectral method, even in this constant-coefficient case, is not a viable approach.

4.3. Lighthill–Westervelt equation

The process of transforming IBVP (40) is similar to that of the shock case, except that additional steps are required due to the spatial variation of the coefficients. For convenience, we recast IBVP (40) as follows:

$$P_{TT} + \mathcal{L}P - \epsilon\hat{\beta}\partial_{TT}(P^2) = 0, \quad (X, T) \in (0, 1) \times (0, T_f), \quad (81a)$$

$$P(0, T) = \mathcal{H}(T) \sin(\pi T), \quad P(1, T) = 0, \quad T \in (0, T_f), \quad (81b)$$

$$P(X, 0) = 0, \quad P_T(X, 0) = 0, \quad X \in (0, 1), \quad (81c)$$

where the differential operator \mathcal{L} is defined by

$$\mathcal{L}P = -V_a^2(X)P_{XX} + \alpha V_a^2(X)P_X,$$

with

$$V_a^2(X) = \exp(2\Re X),$$

and where we let $\Re = -\alpha/2$ for convenience.

4.3.1. Transforming the PDE

As in [21], to homogenize the coefficient of P_{XX} , we define a change of independent variable

$$Y = \phi(X) = \frac{1 - e^{-\mathfrak{R}X}}{1 - e^{-\mathfrak{R}}}.$$

Then, we obtain the transformed differential operator $\tilde{\mathcal{L}}$, defined by

$$\tilde{\mathcal{L}}U(Y) = -\tilde{a}_2 U_{YY} + \tilde{a}_1(Y)U_Y,$$

where

$$\tilde{a}_2 = C^2, \quad \tilde{a}_1(Y) = (\mathfrak{R} + \alpha)C \exp[\mathfrak{R}\phi^{-1}(Y)],$$

with

$$C = \left[\int_0^1 \exp(-\mathfrak{R}X) dX \right]^{-1} = \frac{\mathfrak{R}}{1 - \exp(-\mathfrak{R})},$$

being the homogenized wave speed.

Next, as in Section 4.2.1, we eliminate the coefficient of U_Y , which yields the final form of our spatial differential operator,

$$\tilde{\mathcal{L}}U = -\tilde{a}_2 U_{YY} + \tilde{a}_0(Y)U, \quad (82)$$

where

$$\tilde{a}_2 = C^2, \quad \tilde{a}_0(Y) = \frac{\tilde{a}_1(Y)^2}{4\tilde{a}_2} - \frac{\tilde{a}_1'(Y)}{2}.$$

The transformed problem is now

$$\bar{P}_{TT} + \tilde{\mathcal{L}}\bar{P} - 2\epsilon\hat{\beta}\partial_T(\bar{P}\bar{P}_T) = 0, \quad (Y, T) \in (0, 1) \times (0, T_f), \quad (83a)$$

$$\bar{P}(0, T) = \mathcal{H}(T) \sin(\pi T), \quad \bar{P}(1, T) = 0, \quad T \in (0, T_f), \quad (83b)$$

$$\bar{P}(Y, 0) = 0, \quad \bar{P}_T(Y, 0) = 0, \quad Y \in (0, 1), \quad (83c)$$

where

$$\bar{P}(Y, T) = \psi^{-1}(Y)P(\phi^{-1}(Y), T), \quad \psi(Y) = \exp\left[\int \frac{\tilde{a}_1(Y)}{2\tilde{a}_2} dY\right].$$

4.3.2. Homogenizing the boundary conditions

Next, as in Section 4.2.2, we homogenize the boundary conditions. If we let

$$\bar{P} = U + F,$$

then IBVP (83) becomes

$$U_{TT} + \tilde{\mathcal{L}}U - 2\epsilon\hat{\beta}\partial_T\{UU_T + U_T F + U F_T\} = G, \quad (Y, T) \in (0, 1) \times (0, T_f), \quad (84a)$$

$$U(0, T) = 0, \quad U(1, T) = 0, \quad T \in (0, T_f), \quad (84b)$$

$$U(Y, 0) = -F(Y, 0), \quad U_T(Y, 0) = -F_T(Y, 0), \quad Y \in (0, 1), \quad (84c)$$

where

$$G = -F_{TT} - \mathcal{L}F + 2\epsilon\hat{\beta}\partial_T\{FF_T\}.$$

The functions $F(Y, T)$ and $G(Y, T)$ satisfy the following conditions for $T > 0$:

- $F(0, T) = \mathcal{H}(T) \sin(\pi T)$, $G(0, T) = 0$,
- For $Y \geq \ell$, $F(Y, T) = 0$, $F_Y(Y, T) = 0$, $G(Y, T) = 0$, where ℓ is chosen to be 1/2 in our implementation.

The computation of F and G proceeds as described in Section 4.2.2.

4.3.3. Numerical solution via KSS

A second-order KSS method is then applied to IBVP (84), almost exactly as described in Sections 4.2.3 and 4.2.4. That is, we use the KSS method to approximate

$$\mathbf{r}(T_{n+1}) = \phi_0(J\Delta T)\mathbf{r}(T_n) + \Delta T\phi_1(J\Delta T)\mathbf{c}_n, \quad (85)$$

where $T_n = n\Delta T$ and

$$J = \begin{bmatrix} 0 & \mathbb{I} \\ -\tilde{\mathcal{L}} & 0 \end{bmatrix}, \quad \mathbf{r} = \begin{bmatrix} U \\ U_T \end{bmatrix}, \quad \mathbf{c}_n = \begin{bmatrix} 0 \\ b(Y, T_n) \end{bmatrix},$$

to solve the PDE

$$U_{TT} = -\tilde{\mathcal{L}}U + b(Y, T_n), \quad (86)$$

where

$$b(Y, T_n) = G(Y, T_n) + 2\epsilon\hat{\beta}Q(Y, T_n), \quad Q = \partial_T\{UU_T + U_T F + UF_T\}. \quad (87)$$

One substantial difference from the shock case is that we also need to discretize U_{TT} to compute Q . At the n th time step, this is accomplished by

$$\partial_{TT}\mathbf{U}_N^n \approx S_N^{-1} \left[\frac{\partial_T \hat{\mathbf{U}}_N^n - \partial_T \hat{\mathbf{U}}_N^{n-1}}{\Delta T} \right], \quad \hat{\mathbf{U}}_N^n = S_N \mathbf{U}_N^n.$$

Prior to taking the inverse sine transform, the above difference quotient is regularized to eliminate Gibbs' phenomenon, as is done for the time derivative of the solution. This is discussed further in Section 4.5.

The same KSS method described in Section 4.2.4 is used to approximate Eq. (85). This calls for approximating matrix functions of $\tilde{\mathcal{L}}_N$, a $N \times N$ matrix that discretizes the operator $\tilde{\mathcal{L}}$ via centered differencing. For this task, the formula given in Eq. (79) is again employed, with interpolation points

$$\lambda_{1,k} = 0, \quad \lambda_{2,k} = a_2(2 - 2\cos(\pi k\Delta Y))/(\Delta Y)^2 + \text{avg}(\bar{a}_0), \quad k = 1, 2, \dots, N, \quad (88)$$

where $\text{avg}(\bar{a}_0)$ denotes the average value of $\bar{a}_0(Y)$ on $(0, 1)$.

4.4. Numerical results for the shock wave case

The sequence shown in Fig. 1 depicts particular instances in the evolution of the W vs. z solution profile in the case of IBVP (13), where we have set $W := w/W_0$; it is based on the following parameter values, which, if not dimensionless, are stated in SI units:

$$\vartheta_0 = 300, \quad \gamma = 1.40, \quad c_0 = 347.26, \quad \omega = 2\pi, \quad g = 9.81, \quad \hat{\mu} = 2\hat{\mu}_c \approx 0.0791, \quad (89)$$

where the values taken for γ , g , and c_0 yield $\hat{\mu}_c \approx 0.0395$. We set the right endpoint ℓ of the spatial domain in Eq. (68) to be $40c_0$.

Fig. 1 shows the solution obtained using $N = 262, 144$ grid points and a CFL number of $\frac{c_0\Delta t}{\Delta z} \approx 16.3841$ at times $t = 0.5, 5, 10$. To reduce oscillations due to the Gibbs phenomenon that occurs due to the discontinuity, the Fourier sine coefficients W and W_t are multiplied by Lanczos sigma factors [12]. The sigma factors are raised to appropriate powers p and p° for W and W_t , respectively, to avoid the weak instability that would occur without any smoothing [11]. Less regularization is needed over time. In the implementation $p = (1 - t/t_{\text{end}})^2$ and $p^\circ = 3(1 - t/t_{\text{end}})^2$, where $t_{\text{end}} = 11.0$ is the final time. The numerical solution very closely matches the analytical solution given in Eq. (18). The computed solution also has the correct wave-front location (see Eq. (20)) and the correct shock amplitude (see Eq. (19)) at the wave front, as indicated by the vertical and horizontal red-dashed lines, respectively. Since the numerical solution is also vertical at the wave-front, it correctly captures the jump discontinuity, as desired.

We then repeat the solution process, with two modifications. First, the formula for matrix function-vector products from Eq. (79) is simplified to the formula from Eq. (80). That is, a Fourier spectral method is used to compute the solution, instead of a KSS method. Second, the regularization applied to the KSS method is again used, but with the sigma factors raised to powers $p = p^\circ = 192$, as anything less results in instability. We see in Fig. 2 that the solution is excessively smoothed, so we conclude that this approach cannot produce an accurate solution, at least not without resorting to such effort to fine-tune the regularization that this approach is rendered impractical.

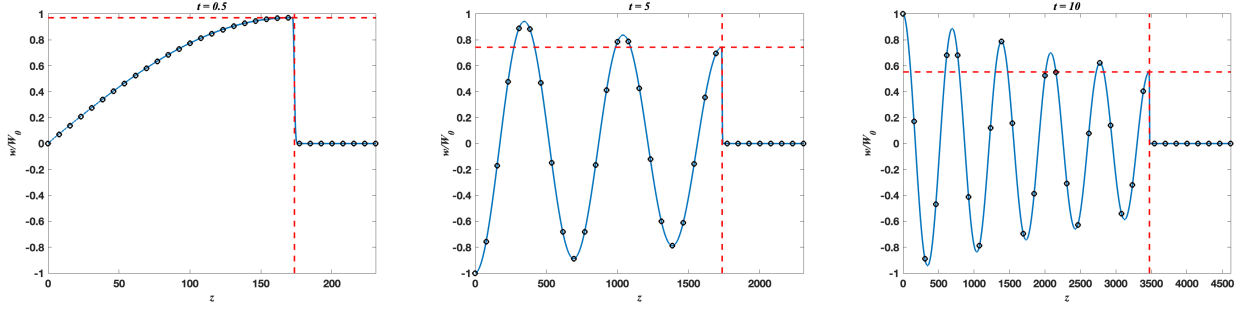


Figure 1: Blue curves: Numerical solution of IBVP (68) computed using the KSS method described in Section 4.2 with $N = 262, 144$ grid points and CFL number 16.3841. The black circles represent the analytical solution; they were generated by numerically evaluating Eq. (18) using MATHEMATICA's (ver. 11.2) `NIntegrate[·]` command. The horizontal and vertical red-dashed lines represent the theoretical shock amplitude values (see Eq. (19)) and wave-front locations (see Eq. (20)), respectively.

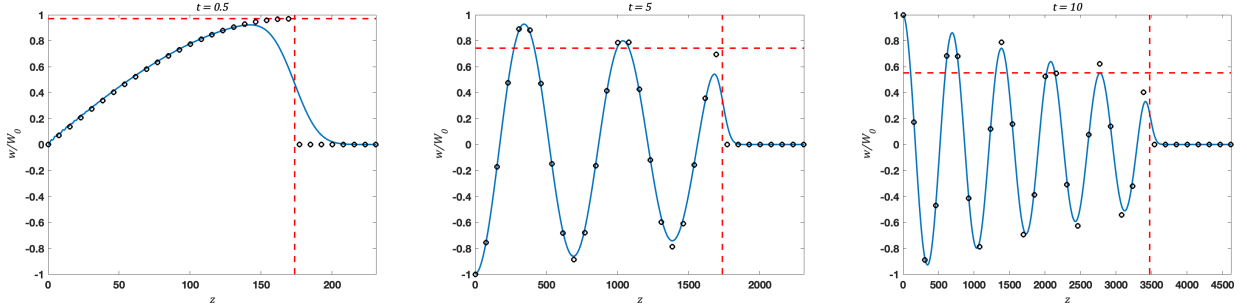


Figure 2: Blue curves: Numerical solution of IBVP (68) computed using the Fourier spectral method described in Section 4.2 with $N = 262, 144$ grid points and CFL number 16.3841, with Eq. (79) replaced by Eq. (80). The black circles represent the analytical solution; they were generated by numerically evaluating Eq. (18) using MATHEMATICA's (ver. 11.2) `NIntegrate[·]` command. The horizontal and vertical red-dashed lines represent the theoretical shock amplitude values (see Eq. (19)) and wave-front locations (see Eq. (20)), respectively.

4.5. Numerical results for the Lighthill–Westervelt equation case

The sequence shown in Fig. 3 depicts the solution of IBVP (81) based on the following *dimensionless* parameter values:

$$\gamma = 1.40, \quad \beta = 1.2, \quad \epsilon = 0.35, \quad (90)$$

with $\alpha = \alpha^*$, where α^* is as defined in Eq. (54). This yields $\alpha = \alpha^* \approx 0.156451$ and $T_f = T_\infty = T_1 \approx 1.04015$. The solution is plotted at $T \approx 0.3, 0.6, 0.98617$, where $X = \Upsilon(0.98617) \approx 0.95$

The blue curves were obtained via KSS using $N = 262, 144$ grid points and a CFL number of $\frac{\Delta T}{\Delta X} = 10$. Oscillations due to the Gibbs phenomenon are addressed as in the shock wave case, except that the regularization is applied to P_T and P_{TT} , whereas P does not need to be regularized as it remains continuous. Also, unlike the shock wave case, the Lanczos sigma factors are raised to a power that *increases* with time, due to the ‘shocking-up’ that occurs. More precisely, for the indicated grid size and CFL number, the Lanczos sigma factors for the Fourier sine transforms of P_T and P_{TT} are raised to powers ϖ^\diamond and $\varpi^{\diamond\diamond}$, respectively, where $\varpi^\diamond = 1536(T/T_{\text{end}})$ and $\varpi^{\diamond\diamond} = 16384(T/T_{\text{end}})^2$, where $T_{\text{end}} = 0.98617$. It can be seen that the slopes of the KSS solution profiles at the wave-fronts match the analytically-derived values (see Eq. (47)).

Next, the sequence shown in Fig. 4 depicts the solution of the same problem, with the same parameter values as in Eq. (90), except now $\epsilon = 0.4$; this increase in ϵ , beyond the value of ϵ^* , yields $\alpha = \alpha^* \approx -0.200618$ and $T_f = T_\infty = T_1 \approx 0.951481$. The solution is plotted at $T \approx 0.3, 0.6, 0.90614$, where $X = \Upsilon(0.90614) \approx 0.95$. The numerical solution is obtained using the same method, with the same discretization and regularization parameters. Again, it can be seen that the slopes of the KSS solution profiles at the wave-fronts match the analytically-derived values (see Eq. (47)). Furthermore, on comparing the former and latter figures we see that P exhibits growth (resp. damping) for

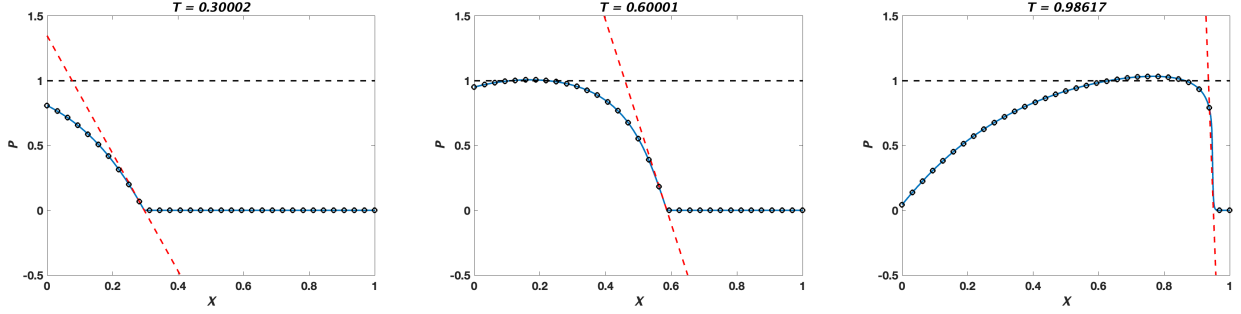


Figure 3: Blue curves: Numerical solution of IBVP (81) based on the parameters given in Eq. (90), computed using the KSS method described in Section 4.3 with $N = 262,144$ grid points and CFL number 10. The black circles represent the solution computed using FDS (B.3) with $M = 4,096$ and CFL number $\delta \approx 0.5201$ (see Eq. (B.4)). The red-dashed lines are plots of $(X - \mathcal{Y}(T))\|P_X\|(T)$; they represent the tangent lines to the solution profiles at the wave-front $X = \mathcal{Y}(T)$.

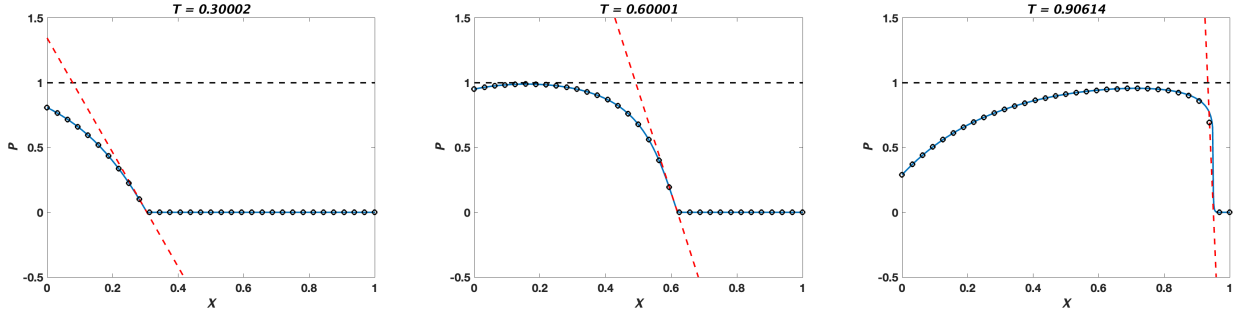


Figure 4: Blue curves: Numerical solution of IBVP (81) based on the parameters given in Eq. (90), except here $\epsilon = 0.4$, computed using the KSS method described in Section 4.3 with $N = 262,144$ grid points and CFL number 10. The black circles represent the solution computed using FDS (B.3) with $M = 4,096$ and CFL number $\delta \approx 0.4757$ (see Eq. (B.4)). The red-dashed lines are plots of $(X - \mathcal{Y}(T))\|P_X\|(T)$; they represent the tangent lines to the solution profiles at the wave-front $X = \mathcal{Y}(T)$.

$\alpha > 0$ (resp. $\alpha < 0$); this behavior is not unexpected, based on the results presented in Ref. [16, § 5.4], because the sign of the coefficient of P_X in Eq. (40a) is the same as $\text{sgn}(\alpha)$.

In concluding this subsection we call attention to the following: While they show excellent agreement for the T -values taken in the left and center panels, in the right panel of Fig. 4 we see a clear discrepancy between the KSS solution profile and the (selected) points from a data set generated by FDS (B.3) near $(\mathcal{Y}(T_{\text{end}}), T_{\text{end}})$. The likely explanation for this lack of agreement can be seen in the right panel of Fig. 5, wherein the tangent line has been omitted for clarity. There, one observes that the FDS (B.3)-based solution profile, which is the result of plotting all points in the aforementioned data set, exhibits high-frequency oscillations near $(\mathcal{Y}(T_{\text{end}}), T_{\text{end}})$, i.e., in exactly the same location where the disagreement occurs.

4.6. Comparison with Krylov subspace methods

To conclude this section, we modify our method for solving Eq. (81) by using Lanczos iteration to compute any required matrix function-vector products. Recall from Section 4.3.3 that $\tilde{\mathcal{L}}_N$ is the $N \times N$ matrix that is the spatial discretization of the differential operator $\tilde{\mathcal{L}}$ from Eq. (82). To approximate $f(\tilde{\mathcal{L}}_N)\mathbf{u}$ for some N -vector \mathbf{u} and function f , we first apply K iterations of the Lanczos algorithm to $\tilde{\mathcal{L}}_N$ with initial vector \mathbf{u} , which yields an orthonormal basis $\{\mathbf{q}_1, \dots, \mathbf{q}_K\}$ for the K -dimensional Krylov subspace

$$\mathcal{K}(\mathbf{u}, \tilde{\mathcal{L}}_N, K) = \text{span}\{\mathbf{u}, \tilde{\mathcal{L}}_N\mathbf{u}, \tilde{\mathcal{L}}_N^2\mathbf{u}, \dots, \tilde{\mathcal{L}}_N^{K-1}\mathbf{u}\},$$

and a symmetric tridiagonal matrix T_K such that

$$\tilde{\mathcal{L}}_N Q_K = Q_K T_K + \beta_K \mathbf{q}_{K+1} \mathbf{e}_K^T,$$

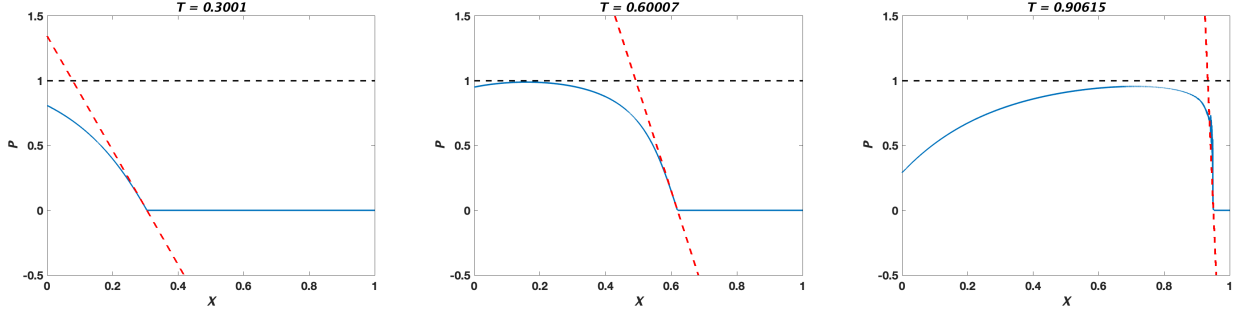


Figure 5: Blue curves: Numerical solution of IBVP (81) using the same parameters values as in Fig. 4; these solution curves were plotted from data sets generated by FDS (B.3) with $M = 4,096$ and CFL number $\vartheta \approx 0.4757$ (see Eq. (B.4)). Again, the red-dashed lines are plots of $(X - \Upsilon(T))\|P_X\|(T)$; they represent the tangent lines to the solution profiles at the wave-front $X = \Upsilon(T)$.

where $Q_K = \begin{bmatrix} \mathbf{q}_1 & \cdots & \mathbf{q}_K \end{bmatrix}$ and β_K is a scalar. Then, we have

$$f(\tilde{\mathcal{L}}_N)\mathbf{u} \approx \mathbf{w}_K = \|\mathbf{u}\|_2 Q_K f(T_K)\mathbf{e}_1. \quad (91)$$

This approach was analyzed in Ref. [13] for the case of $f(\lambda) = e^{-\lambda\tau}$. In our implementation, the number of iterations K is chosen so that convergence of the above approximation is achieved to within some tolerance; more precisely, the relative difference $\|\mathbf{w}_{K+1} - \mathbf{w}_K\|_2 / \|\mathbf{w}_{K+1}\|_2$ is required to be less than 10^{-4} .

Results are presented in Fig. 6. We use the same parameter values as in Eq. (90). The blue curves were obtained using $N = 4,096$ grid points and a CFL number of $\frac{\Delta T}{\Delta X} = 10$. Oscillations due to the Gibbs phenomenon are regularized as they were when using the KSS method, except that regularization is only applied to P_{TT} , and the Lanczos sigma factors are raised to the power $\varpi^\circ = 4,096$. We see that the solution is quite accurate at $T = 0.30022$, but loses accuracy and exhibits some small oscillations at $T = 0.60044$. The method breaks down at $T = 0.73224$, as the Lanczos iteration fails to converge to within the prescribed tolerance. Without the aforementioned regularization, breakdown occurs even earlier. Prior to breakdown, the Lanczos iteration required 11–15 matrix-vector products for each matrix function-vector product, in contrast to the KSS method, which required only one matrix-vector product and three Fourier transforms.

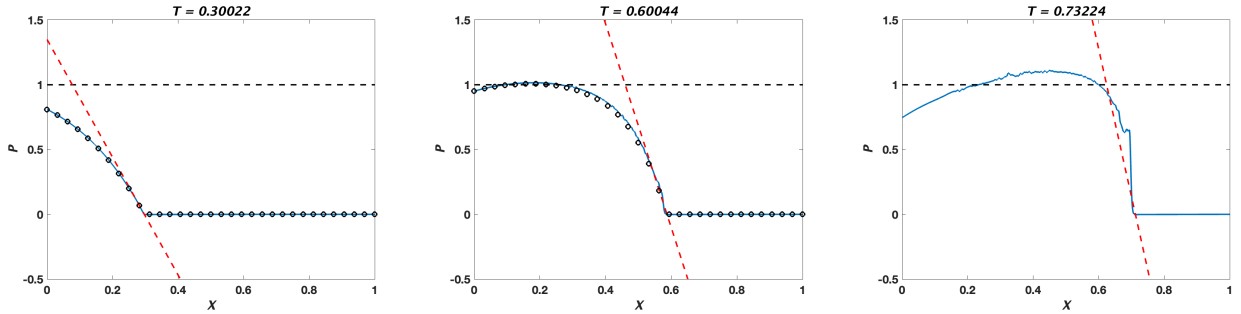


Figure 6: Blue curves: Numerical solution of IBVP (81) based on the parameters given in Eq. (90), computed using the numerical method described in Section 4.3 except with matrix function-vector products approximated as in Eq. (91), using $N = 4,096$ grid points and CFL number 1. The black circles represent the solution computed using FDS (B.3) with $M = 4,096$ and CFL number $\vartheta \approx 0.5201$ (see Eq. (B.4)). The red-dashed lines are plots of $(X - \Upsilon(T))\|P_X\|(T)$; they represent the tangent lines to the solution profiles at the wave-front $X = \Upsilon(T)$.

We also considered the application of an adaptive Krylov iteration from Ref. [26] to compute the matrix function-vector products in the spatial discretization of Eq. (85). The resulting time-stepping scheme is the exponential Euler method [27],

$$\begin{bmatrix} \mathbf{U}_N^{n+1} \\ [\mathbf{U}'_N]^{n+1} \end{bmatrix} = \phi_0(J_N \Delta T) \begin{bmatrix} \mathbf{U}_N^n \\ [\mathbf{U}'_N]^n \end{bmatrix} + \Delta t \phi_1(J_N \Delta T) \begin{bmatrix} \mathbf{0} \\ \mathbf{b}_N^n \end{bmatrix}, \quad J_N = \begin{bmatrix} 0 & I_N \\ -\tilde{\mathcal{L}}_N & 0 \end{bmatrix},$$

where I_N is the $N \times N$ identity matrix and \mathbf{b}_N^n is the spatial discretization of $b(Y, T_n)$ from Eq. (87). Unfortunately, this approach fails to produce a reasonably accurate solution, even at a small time T_n , due to lack of smoothness of the solution.

5. Closure

Extending work that began in Ref. [21], we have further extended the applicability of KSS methods to wave propagation problems that include features such as Rayleigh dissipation, and nonlinear effects that lead to finite-time shock formation. The result is a common framework within which KSS methods can accurately model a variety of wave phenomena, without having to satisfy a CFL condition of the classical type. It has also been demonstrated that KSS methods are capable of producing accurate solutions of problems for which more established methods—Fourier spectral methods in the linear constant-coefficient case, and exponential integrators using Krylov projection in the variable-coefficient or nonlinear case—break down.

Future work will include adding adaptivity to KSS methods, in which residual correction can be used to not only automatically adjust the time step, as in Ref. [8], but also the spatial resolution and any regularization, to prevent contamination of the solution by high-frequency oscillations resulting from discontinuities while also avoiding excessive smoothing. The KSS framework presented in this paper will also be applied to other inhomogeneous media propagation problems of interest, such as those involving dusty gases, poroacoustic drag, and media with multiple layers.

Acknowledgments

B.R. was supported by NASA funding. J.V.L. and P.M.J. were supported by U.S. Office of Naval Research (ONR) funding.

A. Appendix: Results from singular surface theory

Adopting the usual notation convention, we let $\llbracket \mathfrak{F} \rrbracket(t)$ denote the amplitude of the jump discontinuity in the function $\mathfrak{F} = \mathfrak{F}(\xi, t)$ across the singular surface $\xi = \Sigma(t)$; here, we define $\llbracket \mathfrak{F} \rrbracket(t)$ by

$$\llbracket \mathfrak{F} \rrbracket(t) := \mathfrak{F}^- - \mathfrak{F}^+, \quad (\text{A.1})$$

where $\mathfrak{F}^\mp := \lim_{\xi \rightarrow \Sigma(t)^\mp} \mathfrak{F}(\xi, t)$ are assumed to exist, and a ‘+’ superscript corresponds to the region into which Σ is advancing while a ‘−’ superscript corresponds to the region behind Σ .

In this communication, $\xi = \Sigma(t)$ is a smooth planar surface propagating along, and perpendicularly to, the ξ -axis of our Cartesian coordinate system with velocity $V = V(t)$, where $V(t) = d\Sigma(t)/dt$. If $\llbracket \mathfrak{F} \rrbracket(t) \neq 0$ and \mathfrak{F} represents a field variable (e.g., ρ), then $\xi = \Sigma(t)$ is termed a *shock wave* [33, § 54]; if, on the other hand, $\llbracket \mathfrak{F} \rrbracket(t) = 0$ but $\llbracket \mathfrak{F}_\xi \rrbracket(t), \llbracket \mathfrak{F}_t \rrbracket(t) \neq 0$, again assuming that \mathfrak{F} represents a field variable, then $\xi = \Sigma(t)$ is termed an *acceleration wave*⁶.

Lastly, in Section 3 we make use of the following tools from singular surface theory: The 1D version of *Hadamard’s lemma* (see, e.g., Refs. [2], [34, p. 301], and [38, § 174]), specifically,

$$\frac{\mathfrak{d}\llbracket \mathfrak{F} \rrbracket(t)}{\mathfrak{d}t} = \llbracket \mathfrak{F}_t \rrbracket(t) + V\llbracket \mathfrak{F}_\xi \rrbracket(t), \quad (\text{A.2})$$

where $\mathfrak{d}/\mathfrak{d}t$ gives the time-rate-of-change measured by an observer traveling with $\Sigma(t)$ [2]; the (1D) *Maxwell compatibility condition* [38, § 175]

$$\llbracket \mathfrak{F}_t \rrbracket(t) + V(t)\llbracket \mathfrak{F}_\xi \rrbracket(t) = 0, \quad (\text{A.3})$$

which follows from Hadamard’s lemma when $\llbracket \mathfrak{F} \rrbracket(t) = 0$; and the jump product formula [34, p. 302]

$$\llbracket \mathfrak{F}\mathfrak{G} \rrbracket = \mathfrak{F}^+ \llbracket \mathfrak{G} \rrbracket + \mathfrak{G}^+ \llbracket \mathfrak{F} \rrbracket + \llbracket \mathfrak{F} \rrbracket \llbracket \mathfrak{G} \rrbracket. \quad (\text{A.4})$$

⁶For other studies wherein acoustic, or acoustic-like, versions of this class of singular surfaces arise, see, e.g., Refs. [4, 14, 15, 17, 25, 32, 34, 35, 39], and those cited therein.

B. Appendix: Simple explicit scheme for the ihLWE

Generalizing the scheme developed in Ref. [15], wherein acoustic acceleration waves under the constant-coefficient (i.e., homogeneous fluid) version of the LWE were examined, we construct the following simple discretization of Eq. (40a):

$$\begin{aligned} \left(1 - 2\epsilon\hat{\beta}P_m^k\right)\left[\frac{P_m^{k+1} - 2P_m^k + P_m^{k-1}}{(\Delta T)^2}\right] - \exp(-\alpha X_m)\left[\frac{P_{m+1}^k - 2P_m^k + P_{m-1}^k}{(\Delta X)^2}\right] \\ + \alpha \exp(-\alpha X_m)\left[\frac{P_{m+1}^k - P_{m-1}^k}{2(\Delta X)}\right] = 2\epsilon\hat{\beta}\left(\frac{P_m^k - P_m^{k-1}}{\Delta T}\right)^2, \end{aligned} \quad (\text{B.1})$$

where we recall that

$$\hat{\beta} := \beta/\gamma = (1 + 1/\gamma/2). \quad (\text{B.2})$$

In Eq. (B.1), $P(X_m, T_k) \approx P_m^k$, where the mesh points (X_m, T_k) are given by $X_m = m(\Delta X)$ and $T_k = k(\Delta T)$. Additionally, and as dictated by IBVP (40), the spatial- and temporal-step sizes are defined as $\Delta X = 1/M$ and $\Delta T = T_f/(2M)$, respectively, where $M \gg 1$ is an integer.

On solving for P_m^{k+1} , the most advanced time-step approximation, we obtain the explicit finite difference scheme (FDS)

$$\begin{aligned} P_m^{k+1} = 2P_m^k - P_m^{k-1} + \left(1 - 2\epsilon\hat{\beta}P_m^k\right)^{-1} \left[\delta^2 \exp(-\alpha X_m)(P_{m+1}^k - 2P_m^k + P_{m-1}^k) \right. \\ \left. - \alpha\delta(\Delta T) \exp(-\alpha X_m)(P_{m+1}^k - P_{m-1}^k)/2 + 2\epsilon\hat{\beta}(P_m^k - P_m^{k-1})^2 \right], \end{aligned} \quad (\text{B.3})$$

which holds for each $m = 1, 2, 3, \dots, M - 1$ and each $k = 1, 2, 3, \dots, 2M - 1$. Here, we have set

$$\delta := \frac{\Delta T}{\Delta X} = \frac{1}{2}T_f < 1, \quad (\text{B.4})$$

which of course is also the CFL number of our (dimensionless) FDS.

And lastly, the discretized versions of the BCs and ICs of IBVP (40) read

$$P_0^k = \sin(\pi T_k), \quad P_M^k = 0 \quad (k = 0, 2, 3, \dots, 2M) \quad (\text{B.5})$$

and

$$P_m^0 = 0, \quad P_m^1 = P_m^0 \quad (m = 1, 2, 3, \dots, M - 1), \quad (\text{B.6})$$

respectively.

References

- [1] P.G. Bergmann, The wave equation in a medium with a variable index of refraction, *J. Acoust. Soc. Amer.* 17 (1946) 329–333.
- [2] D.R. Bland, *Wave Theory and Applications*, Oxford University Press, 1988, § 6.9.
- [3] B.A. Boley, R.B. Hetnarski, Propagation of discontinuities in coupled thermoelastic problems, *J. Appl. Mech. (ASME)* 35 (1968) 489–494.
- [4] F. Brini, L. Seccia, Acceleration waves and oscillating gas bubbles modelled by rational extended thermodynamics, *Proc. R. Soc. A* 478 (2022) 20220246.
- [5] H.S. Carslaw, J.C. Jaeger, *Operational Methods in Applied Mathematics*, 2nd edn., Dover, 1963.
- [6] A. Cibotarica, J.V. Lambers, E.M. Palchak, Solution of nonlinear time-dependent PDEs through componentwise approximation of matrix functions, *J. Comput. Phys.* 321 (2016) 1120–1143.
- [7] R.M. Corless, et al., On the Lambert W function, *Adv. Comput. Math.* 5 (1996) 329–359.
- [8] H. Dozier, Enhancement of Krylov Subspace Spectral Methods Through the Use of the Residual. Dissertations, 1658 (2019). <https://aquila.usm.edu/dissertations/1658>
- [9] S.J. Farlow, *Partial Differential Equations for Scientists and Engineers*, Dover, 1993.
- [10] G.H. Golub, R. Underwood, The block Lanczos method for computing eigenvalues, *Proceedings of a Symposium Conducted by the Mathematics Research Center, the University of Wisconsin–Madison, March 28–30, 1977, Mathematical Software III (1977)*, pp. 361–377.
- [11] J. Goodman, T. Hou, E. Tadmor, On the stability of the unsmoothed Fourier method for hyperbolic equations, *Numerische Mathematik* 67(1) (1994) 93–129.

- [12] R.W. Hamming, *Numerical Methods for Scientists and Engineers*, 2nd edn., Dover, 1986.
- [13] M. Hochbruck, C. Lubich, On Krylov subspace approximations to the matrix exponential operator, *SIAM J. Numer. Anal.* 34 (1997) 1911–1925.
- [14] A. Jeffrey, Formation of shock waves in atmospheres with exponentially decreasing density, *J. Math. Appl.* 17 (1967) 380–391.
- [15] P.M. Jordan, C.I. Christov, A simple finite difference scheme for modeling the finite-time blow-up of acoustic acceleration waves, *J. Sound Vib.* 281 (2005) 1207–1216.
- [16] P.M. Jordan, Remarks on acoustic propagation in inhomogeneous fluids: Single-phase shock regularization under the Maxwell model, *Int. J. Non-Linear Mech.* 138 (2022) 103839.
- [17] R.S. Keiffer, P.M. Jordan, I.C. Christov, Acoustic shock and acceleration waves in selected inhomogeneous fluids, *Mech. Res. Commun.* 93 (2018) 80–88.
- [18] H. Lamb, *Hydrodynamics*, 4th edn., Cambridge University Press, 1916.
- [19] J.V. Lambers, Enhancement of Krylov subspace spectral methods by block Lanczos iteration, *Electron. Trans. Numer. Anal.* 31 (2008) 86–109.
- [20] J.V. Lambers, An explicit, stable, high-order spectral method for the wave equation based on block Gaussian quadrature, *IAENG J. Appl. Math.* 38 (2008) 333–348.
- [21] J.V. Lambers, P.M. Jordan, On the application of a Krylov subspace spectral method to poroacoustic shocks in inhomogeneous gases, *Numer. Methods Partial Diff. Eqs.* 37 (2021) 2955–2972.
- [22] R.A. Langel, W.J. Hinze, *The Magnetic Field of the Earth’s Lithosphere: The Satellite Perspective*, Cambridge University Press, 1998.
- [23] N.W. McLachlan, *Modern Operational Calculus*, revised edn., Dover, 1962.
- [24] R.E. Mickens, T. Washington, A note on a positivity preserving hyperbolic NSFD scheme for heat transfer, *J. Difference Eqs. Appl.* 28 (2022) 120–125.
- [25] A. Morro, Acceleration waves in thermo-viscous fluids, *Rend. Sem. Mat. Univ. Padova* 63 (1980) 169–184.
- [26] J. Niesen, W.M. Wright, Algorithm 919: A Krylov subspace algorithm for evaluating the φ -functions appearing in exponential integrators, *ACM Trans. Math. Softw.* 38(3) (2012) 22.
- [27] D. Phan, A. Ostermann, Exponential integrators for second-order in time partial differential equations, *J. Sci. Comput.* 93 (2022) 58.
- [28] A.D. Pierce, *Acoustics: An Introduction to its Physical Principles and Applications*, Acoustical Society of America, 1989.
- [29] B. Rester, J.V. Lambers, Convergence analysis of a Krylov subspace spectral method for the 1-D wave equation in an inhomogeneous medium (submitted).
- [30] P.J. Roache, *Computational Fluid Dynamics*, Hermosa Publishers, 1972, § V-D.
- [31] E. Reiso, Nonlinear equations of acoustics in inhomogeneous, thermoviscous fluids, Technical Report No. 89, University of Bergen, 1991.
- [32] G. Saccomandi, Acceleration waves in a thermo-microstretch fluid, *Int. J. Non-Linear Mech.* 29 (1994) 809–817.
- [33] J. Serrin, Mathematical principles of classical fluid mechanics. In: S. Flügge, C. Truesdell (Eds.), *Handbuch der Physik*, Vol VIII/1, Springer-Verlag, 1959, pp. 125–263.
- [34] B. Straughan, *Stability and Wave Motion in Porous Media*, Applied Mathematical Sciences, Vol. 165, Springer, 2008.
- [35] B. Straughan, Shocks and acceleration waves in modern continuum mechanics and in social systems, *Evol. Eqs. Control Theory (EECT)* 3(3) (2014) 541–555.
- [36] G. Taraldsen, A generalized Westervelt equation for nonlinear medical ultrasound, *J. Acoust. Soc. Amer.* 109 (2001) 1329–1333.
- [37] P.A. Thompson, *Compressible-Fluid Dynamics*, McGraw-Hill, 1972.
- [38] C. Truesdell, R.A. Toupin, The classical field theories. In: S. Flügge (Ed.), *Handbuch der Physik*, Vol. III/1, Springer-Verlag, 1960, pp. 491–529.
- [39] E.K. Walsh, Development of shock waves in atmospheres with density and temperature variations, *Phys. Fluids* 12 (1969) 757–763.